

The superwind of OH26.5+0.6 spatially resolved with MIDI

This chapter is based on the paper

The Mid-IR spatially resolved environment of OH26.5+0.6 at maximum luminosity

*O. Chesneau, T. Verhoelst, B. Lopez, L.B.F.M. Waters, Ch. Leinert, W. Jaffe,
R. Köhler, A. de Koter and C. Dijkstra, 2005, A&A, 435, 563–574*

Abstract: In this chapter, we present observations of the OH/IR star OH26.5+0.6 obtained using the Mid-Infrared Interferometric Instrument MIDI at the European Southern Observatory (ESO) Very Large Telescope Interferometer VLT-I. The emission of the dusty envelope, is spatially resolved by a single-dish Unit Telescope (UT). A deconvolved acquisition image taken at $8.7 \mu\text{m}$ exhibits a strong asymmetry. With the FWHM of the major and minor axis being 286 mas and 214 mas respectively, the axis ratio is 0.75 ± 0.07 . The measured Position Angle (PA) of $95^\circ \pm 6^\circ$ appears to be correlated with the asymmetry already detected in the OH maser emission at 1612 MHz. The emission was also spectrally dispersed at a resolution of 30 from $8 \mu\text{m}$ to $13.5 \mu\text{m}$. We find that the angular diameter increases strongly within the silicate absorption band. Moreover, in interferometric mode, the UT1-UT3 102m baseline was used to detect the presence of the central star. Although these observations were carried out during the phase of maximum luminosity of the object, when the dust shell is more diluted and therefore the chance to detect the central source maximized, no fringes were found. With a detection threshold estimated to be of the order of 1% of the total flux of the source, i.e. 5-8 Jy, this points at very high opacity in the inner regions of the dust shell. We modeled the dusty environment using a spherical radiative transfer code and find good spectral but poor spatial agreement. Especially in the wings of the silicate profile, OH26.5+0.6 is much larger than expected. We argue that this extensive set of constraints suggests the presence of an optically thick disk within the spherical outflow of OH26.5+0.6.

6.1 Introduction

The short transition phase between the end of the Asymptotic Giant Branch (AGB) phase and the formation of a White Dwarf (WD) surrounded by a Planetary Nebula (PN) is still poorly understood. The drastic changes observed in the circumstellar environment (CSE) of AGB and post-AGB stars are particularly puzzling. During the late AGB or early post-AGB evolutionary stages, the geometry of the circumstellar envelope of the vast majority of stars changes from more or less spherical to axially symmetric, as shown by the large number of axisymmetric proto-PNe (PPNe, e.g. [Sahai 2000](#)). As a result, most PNe exhibit axisymmetric structures, ranging from elliptical to bipolar, often with an equatorial waist and (sometimes multiple) jets ([Corradi & Schwarz 1995](#)). It is thought that pure hydrodynamical collimation provided by dense equatorial disks or tori ([Icke et al. 1989](#)), and/or magneto-hydrodynamical collimation ([Chevalier & Luo 1994](#)) can explain the development of the extreme bipolar geometries observed. Whether these equatorial structures can arise in a single star scenario is still strongly debated ([Bujarrabal et al. 2000](#)).

The OH/IR phase In recent years, the advent of infrared spectroscopy has improved our understanding of the AGB and post-AGB evolutionary phase. The IRAS and the ISO infrared telescopes have allowed us to identify many of the dust species present around these stars. Moreover, it became clear that mass loss increases dramatically (by an order of magnitude at least) toward the tip of the AGB in what is called a *superwind* ([Iben & Renzini 1983](#)). In this superwind, the last remains of the hydrogen shell are expelled (see also Chapter 1). Besides the total obscuration of the central star by this oxygen-rich, dusty superwind, OH/IR stars are also characterized by strong OH maser emission ([Wilson & Barrett 1972](#)).

The nature and geometry of the superwind is still to be settled. The geometry of the maser emission coming from the outer parts of the CSE is for many objects well constrained due to the combination of the spatial resolution provided by interferometric techniques and the large extension of the maser (usually a few arcseconds). The observations of the youngest (i.e. more optically obscured) PPNe, where the superwind has just ceased, suggest that asymmetries are already present, often in the shape of bipolar outflows. For an extensive discussion on the appearance of bipolar outflows in OH/IR stars, we refer to [Zijlstra et al. \(2001\)](#).

OH26.5+0.6 OH26.5+0.6 (RAFGL 2205, IRAS 18348-0526) is an extreme OH/IR star. At $10\ \mu\text{m}$, the strong absorption by –mainly amorphous– silicates indicates a large dust column density and hence a very high dust mass loss rate. The ISO spectrum of OH26.5+0.6 has been discussed by [Sylvester et al. \(1999\)](#) and the signature of the crystalline silicates was studied by [Molster et al. \(2002\)](#). On the other hand, OH26.5+0.6 exhibits only weak CO $J = 1 - 0$ and $J = 2 - 1$ emission lines ([Heske et al. 1990](#)). [Justtanont et al. \(1996\)](#), hereafter JU96, suggest this to be evidence for two mass-loss regimes: a superwind in which the mass-loss rate is $10^{-4} M_{\odot}/\text{yr}$ which started recently ($t < 200\ \text{yr}$), and an earlier AGB wind with a mass-loss rate of about $10^{-6} M_{\odot}/\text{yr}$. The integrated mass that was lost during the superwind phase is estimated to be about $0.1 M_{\odot}$.

[Fong et al. \(2002\)](#) reported millimetre CO observations which did not show any significant deviation from spherical symmetry for the envelope of OH26.5+0.6. Nevertheless, it must be

pointed out that the source is mainly unresolved at this wavelength. By contrast, it is one of the brightest and most asymmetric OH maser sources known among AGB stars, with an average size of 2–3 arcsec and a preferential axis of symmetry oriented approximately east-west (Baud 1981; Te Lintel Hekkert et al. 1989; Bowers & Johnston 1990). The major question here is whether the observed asymmetry is due to an actual asymmetric density distribution at the location of the maser, or due to an asymmetric illumination (see also Section 6.5)

Unfortunately, the superwind itself is difficult to resolve spatially in the IR by single-dish telescopes. Even more complicating is the large variation of the total luminosity with time. This causes both changes in apparent size and in the actual structure of the inner dust shell. OH26.5+0.6 is a long period pulsating star with a period of about 1559 ± 7 days (Suh & Kim 2002). Taking into account the large variations of the mid-IR flux throughout its pulsation cycle, the published data on its IR spatial extent have to be systematically placed in their temporal context.

Infrared speckle interferometry of OH26.5+0.6 has been performed by Fix & Cobb (1988) close to its maximum luminosity. They estimate an extension of the circumstellar dust shell at $9.7 \mu\text{m}$ (within the strong silicate absorption) of $0.5'' \pm 0.02''$, while outside this feature (at $8 \mu\text{m}$) the shell remained unresolved by their experiment (at most $0.2''$). They have also resolved the environment using the broad N-band filter around phase 0.6 with a detected FWHM of about $0.3''$ (Cobb & Fix 1987). Some asymmetries were reported by Mariotti et al. (1983); Dyck et al. (1984); Cobb & Fix (1987); Fix & Cobb (1988); Starck et al. (1994), but they are within the estimated error bars of the measurements and all together the results are inconclusive, and sometimes contradictory.

We have therefore observed OH26.5+0.6 with the Mid-Infrared Interferometric Instrument MIDI attached to the Very Large Telescope Interferometer (VLTI). This setup offers a spatial resolution in the mid-infrared ranging from the one provided by a single-dish 8m telescope (about 300 mas) to the one provided by the interferometric technique (about 5-10 mas) and a spectral resolution of 30 through the entire N band.

In Section 6.2 we describe the observations and the data reduction procedures, divided into three parts: (1) the single dish acquisition images (Section 6.2.1), (2) the spatial and spectral information of the spectra (Section 6.2.2), and (3) the interferometric signal (Section 6.2.3). In Section 6.3, we model OH26.5+0.6 using a radiative transfer code and compare our model with the observations. Finally, in Section 6.4 we discuss our results.

6.2 Observations and data reduction

We observed OH26.5+0.6 with MIDI (Leinert et al. 2003a,b), the Mid-IR recombiner of the VLT-I. The VLT-I/MIDI interferometer operates as a classical Michelson stellar interferometer to combine the light (N band, $7.5 - 14 \mu\text{m}$) from two VLT Unit Telescopes (UTs). The observations presented here were conducted in the night of the 14 June 2003. The telescopes Antu (UT1) and Melipal (UT3) were used, separated by 102 m and with the baseline oriented 40° (E of N). The observing sequence is described extensively in Przygodda et al. (2003).

6.2.1 Images

The images have been recorded using the MIDI star acquisition modes called Default_Chop and Acquisition_chop with the $8.7 \mu\text{m}$ filter. The Acquisition_chop mode is the first template used after the pointing to test if the target is within the MIDI Field-Of-View (FOV) (diameter of about $3''$) and to perform a fine pointing. The chopping mode ($f=2$ Hz, angle -90 degree) is used to visualize the star, which is not perfectly centered in the first image, and centered in a second step. The number of frames recorded per image is generally about 2000 and the exposure time is by default 4 ms in order to avoid background saturation. If the result of the template is not satisfactory, the procedure is started again. It must be pointed out that no nodding sequences are performed: the sky is removed by chopping only. For some stars for which the coordinates are not well-defined, it might be difficult to get the star directly in the MIDI FOV at the first attempt. This was the case for OH26.5+0.6. Therefore, the Default_Chop is used instead. In this mode, images are recorded only for visualization and the pointing is done by 'hand' between, or sometimes during exposures. In this mode, the number of frames is larger, 15000 frames in our case. The cycle rate is close to 10 ms, so we recorded 15000 frames in about 2.5 min. We stress that MIDI is not intended to be an imager instrument but a long-baseline interferometer. Therefore the majority of the targets (especially the calibrator stars) are totally unresolved by a single 8m telescope, providing a wealth of instrumental Point Spread Function (PSF) acquisitions which can be used for a deconvolution of the OH26.5+0.6 images. The PSF files were recorded with the Acquisition_chop mode and contain 2000 frames (20 s).

Table 6.1 — Journal of observations: acquisition images

Star	Name	Time	Frames	t_{exp}
HD 168454	PSF1	06:02:09	2000	20s
HD 168454	PSF2	06:03:49	2000	20s
HD 168454	PSF3	06:07:34	2000	20s
HD 168454	PSF4	06:08:39	2000	20s
HD 168454	PSF5	06:14:40	2000	20s
HD 168454	PSF6	06:15:50	2000	20s
OH26.5+0.6	star1	06:56:24	10000	100s
OH26.5+0.6	star2	07:00:02	5000	50s
OH26.5+0.6	star3	07:03:46	15000	150s
OH26.5+0.6	star4	07:07:30	15000	150s
HD 177716	PSF7	08:03:11	2000	20s
HD 177716	PSF8	08:04:23	2000	20s

Numerous observations of two calibrator stars (HD 168454 and HD 177716) have been performed before and after the star acquisition. HD 168454 is a bright K3IIIa star exhibiting an IRAS $12 \mu\text{m}$ flux of 62 Jy (the IRAS flux of OH26.5+0.6 is 360 Jy). HD 177716 is a K1IIb giant with an IRAS $12 \mu\text{m}$ flux of 18 Jy. The visual seeing during the HD 168454 exposures was ~ 0.4 arcseconds, during the OH26.5+0.6 exposures it was ~ 0.5 arcseconds and during the HD 177716 around 0.6 arcseconds. The airmass of the three targets ranges from 1 to

1.16. The pixel size on the sky is 98 mas. This scale factor has been defined from the MIDI observations of close visual binaries.

The observations used to obtain a deconvolved image of OH26.5+0.6 are summarized in Table 6.1. They were recorded during the acquisition process and the source location within the FOV can be different for each image. The PSFs (calibrator observations) are generally well centered except for PSF1. Star1 was very far from the FOV center, and the quality of the deconvolution using this observation is very low (but note that the results are consistent with the other measurements).

The deconvolution has been performed using the Lucy-Richardson algorithm (Lucy 1974; Richardson 1972) embedded in the IDL `astrolib` package developed by NASA. Choosing the right iteration number for the Lucy-Richardson algorithm is always a difficult task. Our goal is clearly not to perform the 'best' deconvolution possible, but to increase the spatial resolution of the image which is well resolved by the UTs. The number of iterations used was between 40 and 60. The levels where the different deconvolved images begin to disagree among each other are between 0.3% to 1% of the maximum flux of the image, depending on the quality of the measurement. The level of the differences between PSF1 to PSF6 is about 0.3%. The level of the differences between the PSF of HD 168454 and the ones from HD 177716 can reach 2% for an individual deconvolution but is generally 1%. PSF7 and PSF8 are quite different, with a level of residuals reaching 1.5%.

Table 6.2 — Image size statistics

Name	FWHM X (mas)	rms (mas)	FWHM Y (mas)	rms (mas)
PSF4	148	24	148	24
PSF6	150	28	142	20
PSF8	160	26	166	22
star1	214	8	286	18
star2	210	2	292	14
star3	218	4	296	16
star4	212	2	268	12

A mean deconvolved image was constructed for each observation. A mean deconvolved image was also created using the mean image of star3 and star 4 which were located at the same place in the detector. This reconstructed image is shown in Figure 6.1 to illustrate the quality of the reduction process.

The position of the target for the two other files is different and we did not attempt any shift-and-add procedure to create a single mean image since the useful information is extracted from a fitting procedure of the individual images. We performed a 2D Gaussian fit for each mean deconvolved image which provides the image position, extension and the angle of the long axis in the detector frame. Table 6.2 presents the statistics of this 2D Gaussian procedure and Table 6.3 presents the mean parameters of the deconvolved images.

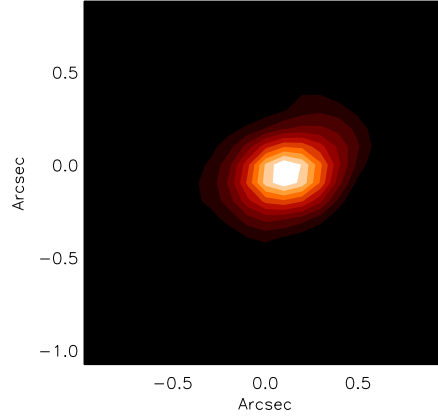


Figure 6.1 — Contours of the mean of star 3 and star 4 deconvolved images. The contour levels are linearly spaced for the double square root of the image $I^{1/4}$. The last contour is equivalent to 25% of the maximum of $I^{1/4}$, i.e 0.4% of the maximum of I . The three last contours are the most susceptible to reconstruction artifacts. The North is up and east is to the left.

Table 6.3 — Deconvolved image parameters. X is oriented along the minor axis, Y along the major axis.

Parameter	Mean	RMS
Mean radius	240 mas	± 14
Mean X axis	214 mas	± 4
Mean Y axis	286 mas	± 6
Mean ratio	0.75	± 0.07
Mean PA angle	95°	$\pm 6^\circ$

The fact that the star is indeed resolved at $8.7 \mu\text{m}$ is beyond doubt, especially after looking at the FWHM of the spectra (Section 6.2.2). Nevertheless, it is necessary to carefully check whether the asymmetry of the image is real or not. The image asymmetry is strong and detected with a large confidence but the PA is almost coincident with the chopping direction. Several checks were performed to substantiate this detection:

1. By way of comparison, the ratio between Y and X extension for the PSFs is 0.997 ± 0.05 . Moreover the position angle of the 2D Gaussian best fitting these PSFs fluctuates randomly. Clearly there is no indication in the PSF files that the chopping had any influence on the image shape.
2. The star is very bright which allowed us to test the deconvolution process in some carefully chosen individual frames (4 ms exposure) taken in the middle of the chopping cycle. The asymmetry is already detectable with a SNR larger than 5 in the best quality frames.
3. We have checked in the literature whether such an asymmetry could have been detected

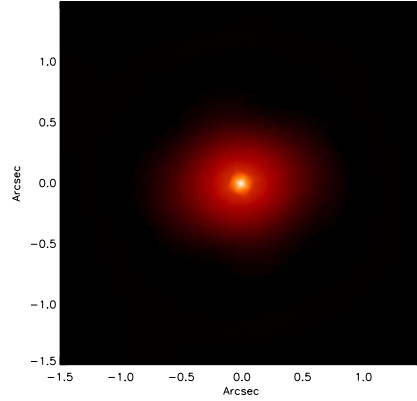


Figure 6.2 — Contours of the reconstructed L band image of OH26.5+0.6 from the speckle observations at the ESO 3.6 m telescope on La Silla (courtesy of Starck et al., private communication).

in the Near-IR by speckle interferometry in the past. Some asymmetries have indeed been seen by [Mariotti et al. \(1983\)](#); [Cobb & Fix \(1987\)](#); [Fix & Cobb \(1988\)](#) in the L ($3.8 \mu\text{m}$), M ($5 \mu\text{m}$) and N ($10 \mu\text{m}$) bands. However the axis ratios reported are not convincing, usually within the estimated error bars of the measurement and not free of any bias as pointed out by [Fix & Cobb \(1988\)](#). Other speckle measurements in the L and M bands are mentioned by [Starck et al. \(1994\)](#), based on observations carried out with the 3.6m telescope of ESO/La Silla at pulsation phase 0.22 (JD=2,448,429). However, the image characteristics are not discussed in that technical paper on the use of the Wavelet Transform in image restoration. In a re-analysis of these data, Starck (private communication) finds a strong asymmetry in the L band with a N-S/E-W ratio of the order of 0.82 ± 0.03 , after removing the unresolved object. It must be stressed that this measurement has been performed by using more than 5 orientations on the sky preventing any direction-dependent bias. The agreement between this reconstructed L band image and our $8.7 \mu\text{m}$ image is convincing as shown in [Figure 6.2](#).

4. Surprisingly, the minor axis reported in this chapter appears to coincide with the putative axis of rotation reported at 1612 MHz by [Bowers & Johnston \(1990\)](#) at a much larger scale (a few arcseconds): both are oriented North-South.

Based on the above considerations, we are convinced that the measured asymmetry is real. *The data are not affected by any bias influencing the shape of the resulting images and this asymmetry can also be seen in other independent data sets.*

6.2.2 Spectrum

The photometry extracted from UT1 and UT3 is intended to calibrate the recorded fringes. Two photometric files are recorded for each target: in the first file, only one shutter is opened

(corresponding to UT1) and the flux is split by the MIDI beam splitter and falls onto two different regions of the detector. The same procedure is then applied to the beam from UT3. The data used to get photometrically calibrated spectra and fringes of OH26.5+0.6 are listed in Table 6.4.

An independent calibration is performed for the individual spectra from each part of the detector and for each telescope. The first step is to read in the photometric data sets, average the frames on the target and the frames on the sky, and subtract the average sky frame from the average target frame. The position of the spectrum is then measured column-wise (a column contains the spatial information) by searching for peaks that are sufficiently high above the background fluctuations. The result is the position and width of the spectrum as a function of wavelength.

We use HD 177716 as absolute flux calibrator (Cohen et al. 1999), taking into account differences in air mass between calibrator and OH26.5+0.6. Then, the calibrated spectra are combined in order to provide a high SNR spectrum. The shape of the spectra from the same telescope agree within 1-2%, but the spectra from two different telescopes can vary by about 5%. This is due to different optical paths which were intrinsically different during the early use of the MIDI instrument with the VLT-I (poor pupil transfer). The temporal flux variations are the dominant source of error for the absolute flux calibration, and variations of 5-20% or even more are routinely observed in the N band¹. The final calibrated spectrum is shown in Figure 6.3, together with the ISO-SWS spectrum for comparison.

Table 6.4— Journal of observations: fringe scans and photometric files

Star	Telescope	Time	Frames
HD 168454	UT1	06:40:47	3000
HD 168454	UT3	06:43:12	3000
OH26.5+0.6	UT1/UT3	07:13:36	12000
OH26.5+0.6	UT1/UT3	07:20:09	9000
OH26.5+0.6	UT1/UT3	07:23:46	9000
OH26.5+0.6	UT1	07:27:51	3000
OH26.5+0.6	UT3	07:29:51	3000
HD 177716	UT1	08:18:44	3000
HD 177716	UT3	08:20:48	3000

We studied the spatial extension of the spectra in the direction of the slit so as to check whether the shell of OH26.5+0.6 is spatially resolved at all wavelengths. A 1D Gaussian fit was performed for each column of each spectrum from the target and the calibrators. The PA of the slit (72°) is close to the PA of the major axis detected in the deconvolved image at 95° . In Figure 6.4 we see that OH26.5+0.6 is well resolved by the 8m telescope.

In order to constrain the true size of the object in the slit direction, we performed a deconvolution on each of the 4 available spectra (two for each telescope). A 1D deconvolution using the Lucy-Richardson algorithm is done column by column using a normalized column

¹Since the pupil location is not fully stabilised, this may be an instrumental effect, but also the atmospheric transmission can vary with time if the weather conditions (water content) change quickly.

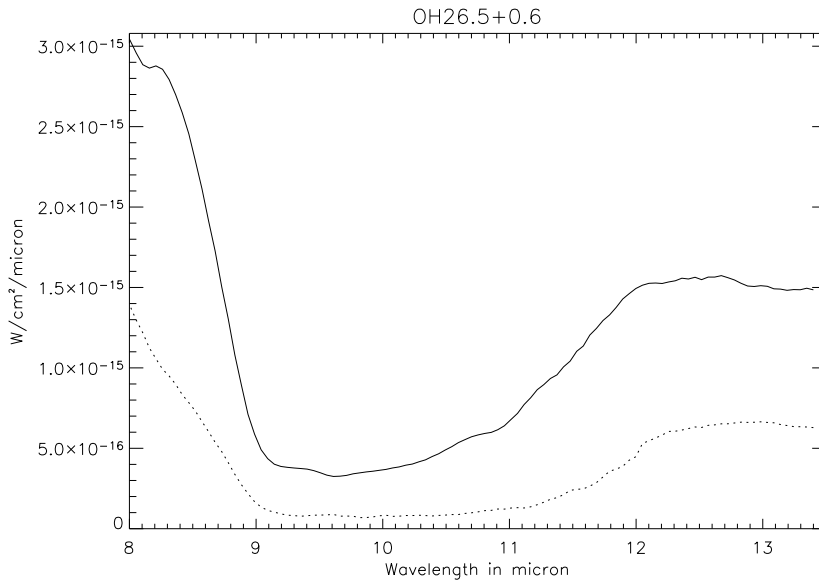


Figure 6.3— Calibrated spectrum from MIDI (solid line) corresponding to the mean flux from UT1 and UT3. The flux is almost 300% higher than the flux observed by ISO, shown with a dotted line. The ISO data have been recorded during a minimum of the light curve (Suh & Kim 2002).

from the calibrators as PSF. The same number of iterations is applied at every wavelengths. There are some minor differences between the shapes provided by UT1 and UT3 which can be attributed to differences in the optical quality of the different light paths. The final FWHM as a function of wavelength from the UT3 spectra is shown in Figure 6.5.

6.2.3 Fringes

Fringes were searched for by repeatedly scanning a large range in optical path difference (OPD) between the two telescopes, using a small instrumental delay line (see Przygodda et al. (2003) for a description of the observing sequence). A mask is created with the average position and width of the spectra recorded in the photometric files for UT1 and UT3. This mask is used to extract the object data from the fringe tracking datasets. Each frame of the fringe data, corresponding to one individual optical path delay (OPD) setting inside a scan, is reduced to a one-dimensional spectrum by multiplying it with the mask and performing the weighted integral over the direction perpendicular to the spectral dispersion. Thereafter, the two – oppositely phased – interferometric output channels of the beam combiner are subtracted from each other. This combines the interferometric modulation of both channels into one signal and at the same time helps subtracting out the background. The few dozen spectra from each scan with the piezo-mounted mirrors are collected into a two-dimensional array with wavelength and OPD as axes. The contents of this array are column-wise Fourier-transformed from OPD to fringe frequency space. As a rule, four of the $\approx 0.05 \mu\text{m}$ wide

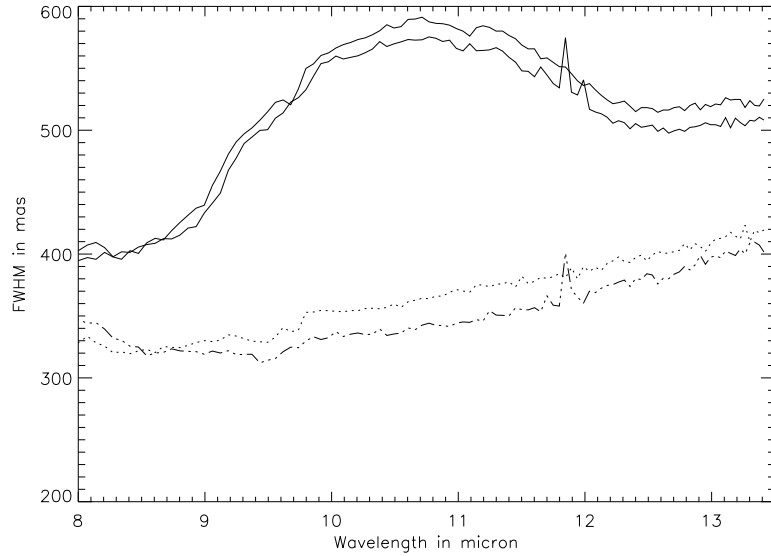


Figure 6.4 — FWHM (in the spatial direction) of the OH26.5+0.6 spectrum from UT1 (solid lines) throughout the wavelength range compared to the FWHM of the unresolved calibrator HD 168454 (dotted lines). There are two lines per target because the MIDI beam splitter is inserted, generating 2 spectra on the detector.

wavelength (pixel) channels were added to improve the signal-to-noise (S/N) ratio. The fringe amplitude for each wavelength is then obtained from the power spectrum at the corresponding fringe frequency.

No correlated flux was detected with the UT1-UT3 projected baseline of 102.4 m at a PA of 39.6° . Based on the first few months of routine observations with MIDI, we can set limits on the amount of correlated flux the instrument is capable of detecting under average weather conditions. For instance, a careful data reduction of the data from NGC 1068 shows that a correlated flux can be confidently detected down to 0.5 Jy for faint objects (Jaffe et al. 2004). For bright objects, visibilities of the order of 1% have been detected for the heavily resolved Herbig star HD 100546 (Leinert et al. 2004), or for the clumpy environment of the supergiant η Car (Chesneau et al. 2005). This number has to be compared to the total photometric flux of OH26.5+0.6 entering the slit, which is about 600-800 Jy. With the 100m baseline, MIDI in interferometric mode is sensitive to the emission coming from any structure smaller than 10 mas with a flux larger than 5-8 Jy.

6.3 Modelling the circumstellar environment

In this section, we compare the observed MIDI N-band spectrum and FWHM profile with a theoretical dust shell model.

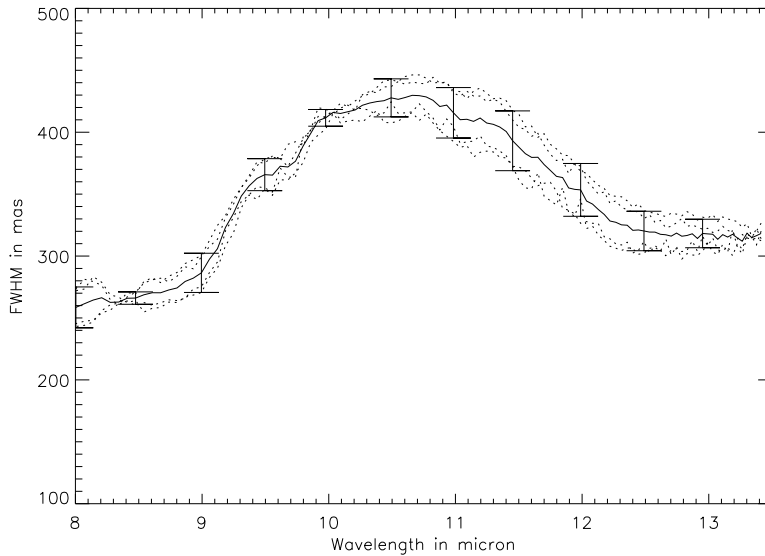


Figure 6.5 — Mean of FWHM curves of the OH26.5+0.6 deconvolved spectra from UT3 (solid line) and the individual deconvolution using different calibrators (dotted lines). The errors bars (spaced by $0.5 \mu\text{m}$ intervals) represent only the scatter of the measurements.

6.3.1 Modelling strategy

Most studies on OH/IR stars, and on OH26.5+0.6 in particular, rely on the interpretation of the observed variable Spectral Energy Distribution (SED) by comparing it to a synthetic SED, computed using a radiative transfer code. In this way, one tries to separate effects of opacity and radial structure in the wind. Unfortunately, fits to the SED are often not unique, especially when deviations from spherical symmetry are taken into account. MIDI, however, provides us with unique spectrally **and** spatially resolved data. The aim of this analysis is to pinpoint the kind of constraints provided by the inclusion of the spectrum *and* the spatial extension of the object in the process of model fitting. We will demonstrate how new information can emerge on the dust content close to the star.

The dust shell is modelled using the proprietary spherical radiative transfer code MODUST (Bouwman et al. 2000; Bouwman 2001). Under the constraint of radiative equilibrium, this code solves the monochromatic radiative transfer equation from UV/optical to millimetre wavelengths using a Feautrier type solution method (Feautrier 1964; Mihalas 1978) in spherical symmetry. The code allows to have several different dust components of various grain sizes and shapes.

Despite the convincing evidence that the envelope of OH26.5+0.6 is not spherical, we begin our analysis assuming spherical symmetry since this is one of the assumptions in the MODUST radiative transfer code. As a first step, we use the SED observed by ISO to determine global envelope parameters. The ISO spectrum, and unfortunately also the IRAS data, were taken

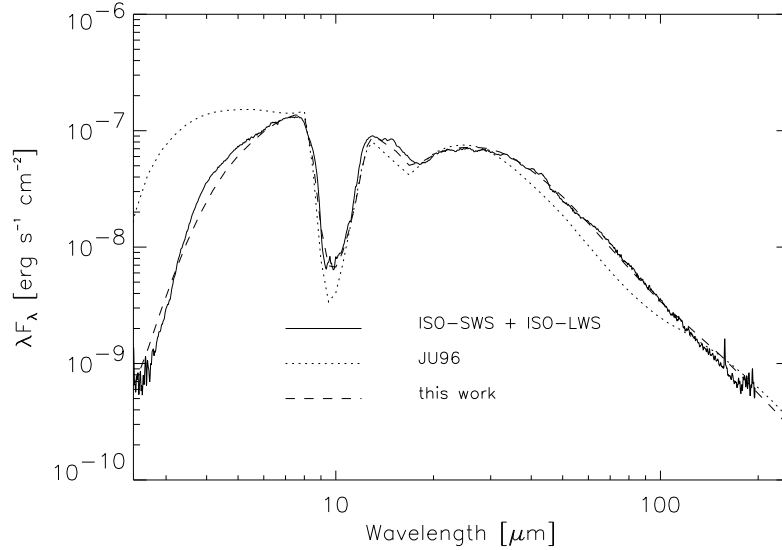


Figure 6.6— Comparison between the ISO spectra (SWS + LWS) and a MODUST model using the JU96 parameters (dotted line) and the same model but with a slightly reduced luminosity of the central star, CDE instead of MIE particles and the inclusion of 3% metallic iron (dashed line). The crystalline features present in the ISO-SWS observation are not included in the model since they have little effect on the model structure (Kemper et al. 2002). The ISO spectrum was dereddened for an interstellar $E(B-V)=0.91$ (Arenou et al. 1992) using the interstellar extinction law of Savage & Mathis (1979) and the theoretical extension to longer wavelengths of Steenman & The (1989, 1991).

close to the phase of *minimum luminosity* (Suh & Kim 2002). The model fit therefore provides constraints on the physical parameters of the dust shell close to *minimum luminosity*. The model fit parameters are compared to the parameters published by JU96, who also mainly scaled their spectrophotometric data to the minimum phase.

Thereafter, we adapt our model to the MIDI data taken at *maximum luminosity*, i.e. we try to fit the MIDI spectrum by performing small modifications to the minimum light model. These modifications are based on “physical” parameter changes when going from minimum to maximum light. As soon as a satisfactory fit is reached for the MIDI spectrum, we evaluate the spatial distribution of the flux predicted by the model and compare it with the extension at each wavelength measured by MIDI.

Throughout this analysis, we will adopt a distance of 1.37 kpc for OH26.5+0.6. We note that distances to AGB stars are notoriously uncertain, and OH26.5+0.6 is no exception. Since we are mainly interested in the variation of apparent size with wavelength, and not the absolute values, this poorly known distance is not a reason for concern.

6.3.2 SED fit of OH26.5+0.6 at minimum luminosity

Justtanont et al. (1996), hereafter JU96, constructed a model for OH26.5+0.6 based on a large collection of photometric, spectroscopic and CO-line measurements. Their 2-component model (a very thick inner shell, due to a recent superwind, surrounded by a tenuous AGB wind) shows that the near–mid IR is dominated by the superwind region. Most of their study is based on fluxes measured at minimum light, and hence should be applicable to the ISO-SWS spectrum, also obtained around minimum light (JD=2,450,368, phase 0.47). The

Table 6.5 — In column 2, the model parameters from Justtanont et al. (1996) (JU96) are given. The 3rd column specifies our model parameters obtained by fitting the ISO spectrum the ISO data (minimum light, JD=2,450,368, phase 0.47). The parameters obtained from fitting the MIDI data (maximum light, JD=2,452,804, phase 0.06) under the assumption of a larger inner radius, are given in column 4.

Parameter	JU96	Minimum	Maximum
T_{eff} (K)	2200	1900	2400
R_* (R_\odot)	862	850	850
Dist. (kpc)	1.37	1.37	1.37
Superwind			
R_{in} (R_*)	7.5	10	30
R_{out} (cm)	8×10^{15}	8×10^{15}	8×10^{15}
\dot{M} (M_\odot/yr)	5.5×10^{-4}	5.5×10^{-4}	8.5×10^{-4}
AGB wind			
R_{in} (cm)	8×10^{15}	8×10^{15}	8×10^{15}
R_{out} (cm)	5×10^{18}	5×10^{18}	5×10^{18}
\dot{M} (M_\odot/yr)	$1. \times 10^{-6}$	1.4×10^{-5}	1.4×10^{-5}

superwind hypothesis is confirmed by the ISO-SWS spectrum, which shows very little far-IR flux w.r.t. the depth of the $10 \mu\text{m}$ feature. Assuming a density distribution going as r^{-2} this can be modelled only by cutting the shell fairly close to the star (at a few hundred stellar radii instead of a few thousand).

In Figure 6.6, we show the ISO spectrum compared to the JU96 model (dotted line), calculated with MODUST and scaled to the ISO flux level (parameters listed in Table 6.5). Some clear discrepancies appear: the near-IR flux is strongly overestimated and the silicate absorption feature at $9.7 \mu\text{m}$ is too deep and narrow. In order to improve the quality of the fit, we made the following adjustments: (1) the slope in the near-IR ($4\text{--}8 \mu\text{m}$) is strong evidence for the presence of (about 3% of) metallic iron, as is the case for OH127.8+0.0 (Kemper et al. 2002), (2) the width and location of the $9.7 \mu\text{m}$ feature indicate that CDE theory (CDE, Continuous Distribution of Ellipsoids) is to be preferred over spherical dust particles (MIE theory), and (3) because of the larger opacity of our model in the near IR, the total luminosity should be somewhat lower than proposed by JU96 (see also Table 6.5). Since the dust shell is so optically thick, only the total luminosity of the central star influences the final SED: it is not possible to differentiate between changes in temperature or radius of the central star. In the following, we choose to change the temperature, at a constant radius.

We obtain a satisfying fit to the ISO spectrum by reducing the stellar temperature to 1900 K². The comparison of our best-fitting model with the ISO spectrum is also shown in Figure 6.6. The general shape is approximately good. Most of the discrepancies beyond 10 μm can be attributed to a lack of crystalline dust in our model. These crystalline features are probably due to a few percent of enstatite and forsterite. Since these do not influence the model structure significantly (Kemper et al. 2002, their opacities outside the resonance bands are very similar to those of the amorphous material), a detailed fitting of their spectral features is beyond the scope of this work. We also remark that despite the inclusion of metallic iron, the match to the near-IR slope is still not perfect.

6.3.3 Comparison with the MIDI data

Going from minimum (the ISO spectrum) to maximum light (the MIDI data), our model will have to explain the following new MIDI observations:

1. The MIDI N-band spectrum taken close to maximum light (JD=2,452,804, phase 0.06) through an 0.588 arcsecond wide slit.
2. The spatial extent of the spectrum. We limit ourselves to the comparison of the FWHM provided by a fit of the PSF-deconvolved MIDI spectrum by a 1D Gaussian with a similar fit of the model intensity profiles. The intensity distribution of OH26.5+0.6 on the sky is likely more complex than a simple Gaussian. However, it turned out to be difficult to disentangle imperfections in the imaging quality resulting from the many reflections in the VLT-I optical train from those intrinsic to the source, especially at lower intensity levels. The slit was oriented at PA=72°, i.e. close to the maximum extension of the object.
3. The negative detection of fringes by MIDI in interferometric mode. The constraints provided by this observational fact should not be underestimated. At maximum luminosity, the dust shell opacity is *at its minimum*. It is quite difficult from a model of the MIDI spectrum alone to disentangle models which are almost optically thin in the wings of the silicate features to the ones more optically thick. The MIDI observations definitely discard any models of OH26.5+0.6 for which the central star is visible with a (correlated) flux larger than 3–6 Jy through the shell at any wavelength located between 8 μm and 13.5 μm .

The MIDI observations were done very close to maximum light, resulting in an absolute flux level which is more than twice as high as at minimum light, i.e. the flux of the ISO spectrum. In order to adapt the model at minimum luminosity to the MIDI data at maximum luminosity taken through the narrow slit, we must increase the total luminosity from 7500 L_{\odot} to about $1.9 \times 10^4 L_{\odot}$ (Figure 6.7). This luminosity is still significantly below that predicted from the light curve presented by Suh & Kim (2002): 30 000 L_{\odot} .

We already discussed above that it is impossible from these data to derive the actual change in temperature and radius of the central star. Since dynamical model atmospheres for Mira

²Whether this value is physically realistic is not clear, but given the limited meaning of the *effective temperature* in pulsating evolved stars with extended atmospheres, this is not a reason for concern

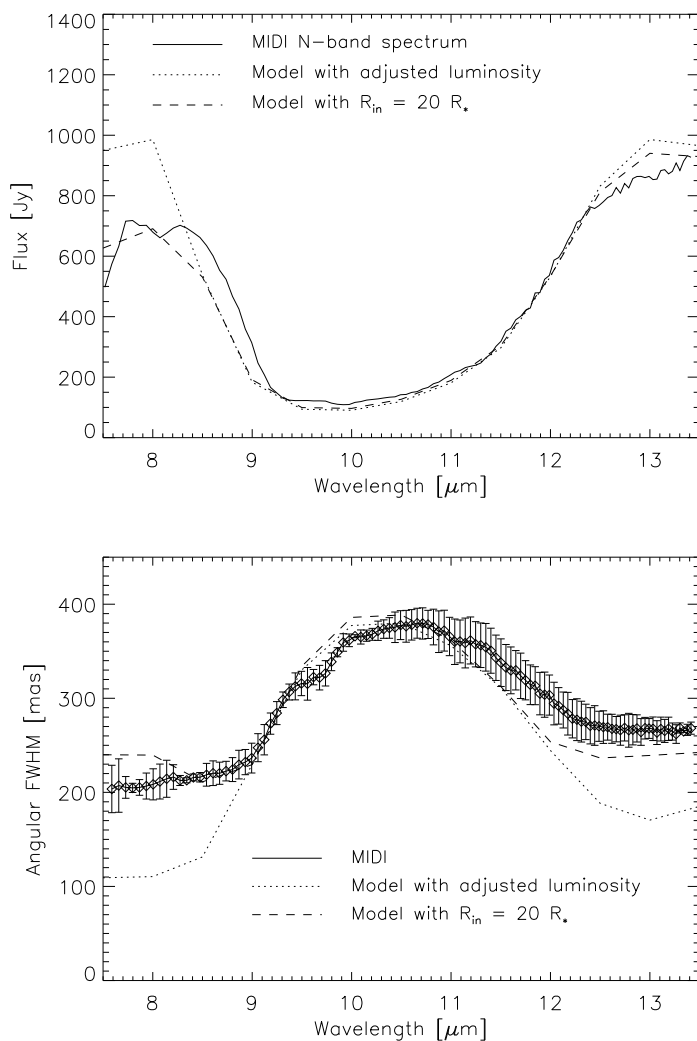


Figure 6.7 — Upper panel: Comparison between the MIDI spectrum (solid line, dereddened as in Figure 6.6), the spectrum resulting from our ISO-tuned model but with increased central star luminosity (dotted line), and a model with a larger inner radius to match the observed FWHM (dashed line, see text for details). Lower panel: Comparison between the FWHMs of the intensity profiles coming from the ISO-tuned model with a more luminous central star and the MIDI FWHMs (dotted line). The predicted variation of diameter with wavelength is much larger than the one observed. Mainly the size at minimum optical thickness of the shell model (at 8.5 and 13.5 μm) does not agree. This discrepancy can be solved with a larger inner radius (dashed line).

variables now predict that the maximum light coincides with minimum radius and maximum temperature (Bessell et al. 1996), we chose to increase the total luminosity by an increase of

the stellar temperature while keeping the radius fixed. Below, we confront this model with the MIDI FWHM observations.

Figure 6.8 shows the spatial intensity profiles according to our ISO-tuned model adapted to the higher total luminosity at the time of the MIDI observations. The profiles at 8.5 and 13.5 μm correspond to a fairly low optical thickness of the shell and thus the central star is not totally obscured. However, the amount of correlated flux by the central star is at most a few Jansky and hence close to the detection limit of MIDI (1 % or 5-8 Jy). At 10.5 μm , the shell reaches an optical thickness of more than 10, resulting in the Gaussian intensity profile.

The FWHMs determined from these intensity profiles range from 100 mas to 370 mas (Figure 6.7), clearly showing that if only the opacity by amorphous olivines were to determine the observed diameter, the variations with wavelength would be much larger than what is found with MIDI. The maximum size appears to compare reasonably well with the model (though with a slightly different wavelength of maximum) and hence is compatible with the superwind size of JU96. More precisely, under the assumption of a Gaussian intensity profile, we can put a lower limit to the radius of the superwind region of about 800 mas, which corresponds to a radius of 8×10^{15} cm or 250 AU at 1.37kpc.

The discrepancy between the spatial extent of the model and the observed size of the dust shell near 8 and 13 μm can be resolved if the inner radius of the dust shell is increased. In such a scenario, the minimum size seen is mainly determined by the inner radius of the dust shell: at the wavelengths of low optical depth, the intensity profile is not at all Gaussian (Figure 6.8). In this way, the observed diameter in the wings of the 9.7 μm feature can be simulated with inner radius of about 30 R_{\odot} (Figure 6.7). This model requires a slightly higher mass loss ($8.5 \times 10^{-4} M_{\odot}$) to keep the quality of the spectral fit. Unfortunately, this model predicts a correlated flux using the 102 meter UT1-UT3 baseline which is 5 times the upper limit imposed by the non-detection of fringes in the interferometric signal, under the assumption that the central star has a typical AGB temperature below 4000 K (see also Section 6.4).

At first sight, an alternative solution would be to introduce in the superwind a source of opacity with only a modest wavelength dependence, which would dominate over the silicate dust opacity near 8 and 13 μm . This extra source of opacity would increase the observed size in the wings of the silicate profile, and reduce the correlated flux from the central star to below detectable levels. It could either be gas-phase molecular opacity or dust. However, by introducing such an ad-hoc source of opacity, the spectral fits become unacceptably poor, because the depth of the silicate feature can no longer be reproduced.

In summary, we conclude that the spectral and spatial data of OH26.5+0.6 can be understood in the framework of a spherically symmetric shell, with dust components that are also shown to be present in other OH/IR stars. The outer radius of the dust shell agrees well with the one estimated by JU96 as the radius of the onset of the superwind. The spatial data near 8 and 13 μm force us, in the context of spherical symmetry, to use as inner radius of the dust shell a distance of about 30 stellar radii. However, this results in a predicted correlated flux using the 102 meter UT1-UT3 baseline which is 5 times the upper limit imposed by the non-detection of fringes.

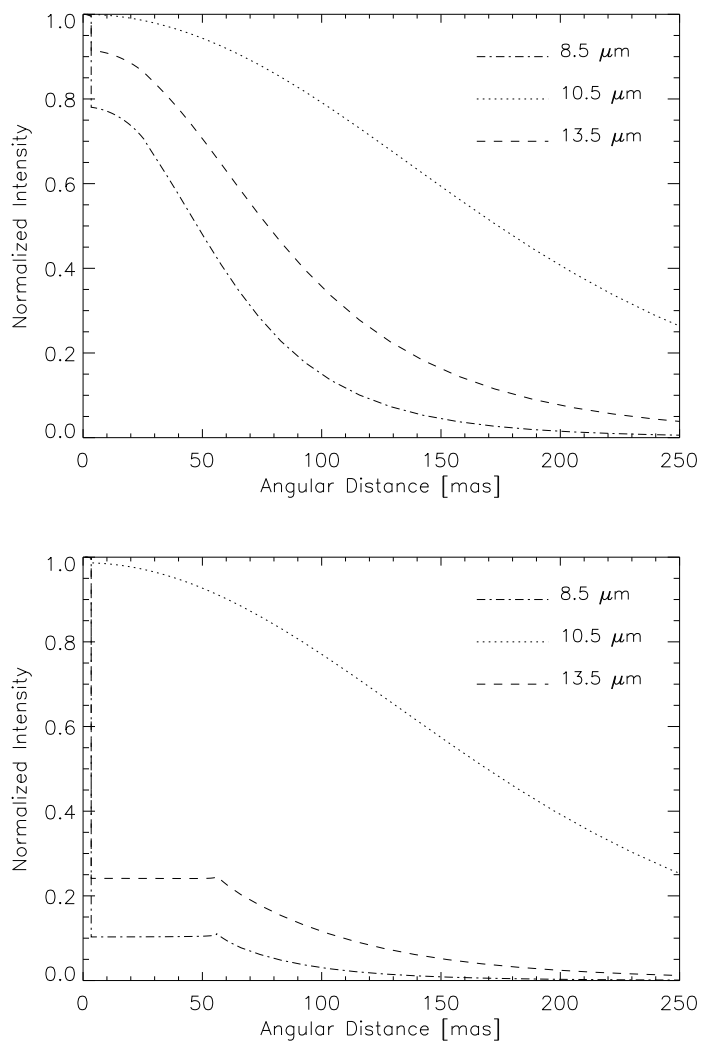


Figure 6.8— Upper panel: Normalized intensity profiles for our model at maximum luminosity. In the wings of the $9.7 \mu\text{m}$ profile (at 8.5 and $13.5 \mu\text{m}$), the shell optical thickness is only about 2 and the central star is visible. At $10.5 \mu\text{m}$, the shell reaches an optical thickness of more than 10, resulting in the Gaussian intensity profile. Lower panel: Normalized intensity profiles for our model at maximum luminosity with an increased inner radius. For these intensity profiles, the inner radius is determining the observed size of the object at wavelengths of low opacity.

6.4 Discussion

Let us first discuss the need for a large inner dust radius under the assumption of spherical symmetry. Thereafter, we present/discuss other possibilities to explain the 1-D data (FWHM,

negative detection of fringes). We also discuss the asymmetry found in the acquisition images and the limits on clumping in the envelope imposed by the negative detection of fringes.

6.4.1 Nature of the large inner dust radius

While a large inner radius of the dust shell forms a simple solution to the initial discrepancy between model and observations, it appears to be in contradiction with the limits set by the interferometric measurement: the negative detection of fringes. This model has little opacity at 8 micron ($\tau_{8\mu m}$ is of the order of 1), and hence the amount of correlated flux from the central object would be about 5 times the detection limit of MIDI, if the central star is still at an AGB temperature. Only if the central star is either considerably warmer (above 4500 – 5000 K) or much cooler (~ 500 K), can the correlated flux be below detectable levels. This is demonstrated in Figure 6.9: under the assumption of a given total luminosity, in this case $1.9 \times 10^4 L_{\odot}$, there is a 1-to-1 relationship between diameter and temperature. For each combination of diameter and temperature we calculated the correlated flux at a projected baseline of 102.4 m, assuming a dust opacity of $\tau = 1$ or 2 at 8 μm . From this figure, it is clear that, if we assume the dust shell to have a large inner radius in which case the dust opacity at 8 μm is only about unity, then the central object can be either very large and cool (only a few hundred Kelvin), or rather hot, i.e. warmer than 4000 K.

In addition, such a large inner radius is not compatible with our current understanding of oxygen-rich AGB dust shells: the dust temperature at the inner edge of our dust envelope is only 500-600 K, well below what is believed to be the condensation temperature of olivines (1000 K). Furthermore, one can wonder whether the region between photosphere and olivine dust shell contains other material (dust grains with a higher condensation temperature for instance, like corundum).

Given the constraint that whatever fills this inner region must be quite transparent from 8 to 13 μm ³, several hypotheses can be formulated:

- The inner region is actually (almost) empty. This could indicate that the mass loss has decreased strongly about 30 years ago. This is compatible with the timescales derived from the rings observed around several Post-AGB stars, hinting at episodic mass-loss with periods of a few hundred years, e.g. IRAS 17150-3224 (Kwok et al. 1998), IRC+10216 (Mauron & Huggins 1999), the Egg Nebula (Sahai et al. 1998; Marengo et al. 2001). However, stellar pulsations are quite regular and have been detected over the past 30 years (e.g. Suh & Kim 2002). So, if mass loss stopped, apparently the pulsations did not. This puts into question the relation between pulsations and mass loss for AGB stars in the superwind phase. Interestingly, Monnier et al. (2000) also find that some strongly pulsating AGB stars (e.g. IRC+10216) do not form dust at every pulsation cycle. Together with the possibility that the central star is actually fairly hot, this could also suggest that OH26.5+0.6 is a very early Post-AGB star. However, when the superwind ends, the SiO maser usually disappears quite soon after, while in OH26.5+0.6, the SiO maser is still

³This means optically thin from 7.5 to 9 micron and from 11.5 to 13.5 micron. An optically thick shell ($\tau \simeq 2-3$) is neither compatible with the N-band spectrum, nor with the observed FWHMs.

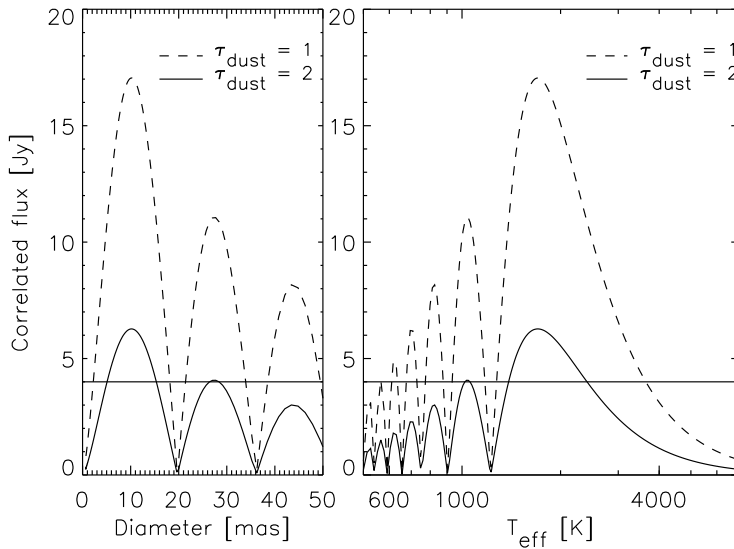


Figure 6.9— Correlated flux at $8 \mu\text{m}$ as a function of central star diameter or temperature, under the assumption of a total luminosity of $1.8 \times 10^4 L_{\odot}$, and seen through an envelope with an optical thickness of either 1 or 2 at $8 \mu\text{m}$. Under the assumption of a large inner radius for the dust shell, in which case the dust opacity at $8 \mu\text{m}$ is only about unity, the negative detection of fringes in the MIDI observations suggests that the central object is either very large and cool (500 K), or fairly hot, i.e. warmer than 4000 K, which would suggest OH26.5+0.6 to be a very recent Post-AGB star.

strong (Nyman et al. 1998). Moreover, this is again hard to reconcile with the observed strong, regular (over the last 25 years) pulsations.

- The mass loss is continuing even today and no condensation of the dust is possible inward of 30 stellar radii when the star is at maximum luminosity. In fact, early dust condensation models by Sedlmayr (1989) have predicted that the dust condenses only when the gas is extremely super-saturated, which happens well below the glass temperature, and would be around 800-600K. Several other studies have previously hinted at the possibility that dust formation in AGBs does not happen close to the star. Danchi et al. (1994) also find some examples of stars with rather detached dust shells, corresponding to timescales of decades, so similar to what we find. However, other stars have inner dust radii much closer to the star.
- The dust gets periodically destroyed (dust evaporation) because the stellar luminosity changes during a pulsation cycle. Some calculations were done by Suh & Kim (2002), but do not predict the required amount of dust destruction to agree with our geometrical model. It is not certain that the net amount of dust created through an entire cycle is stable. This means that the episodic mass loss is a matter of balancing between destruction and formation. Of course, if the dust formation is not large enough to compensate for the evaporation, the inner gap would increase in size over multiple cycles.

Clearly, the negative detection of fringes is a very constraining evidence in this discussion. Since the hypothesis of a hot central star is not compatible with the strong stellar pulsations, the central object must be very large and cool. An attractive explanation could be the inclusion of molecular opacities. Growing evidence of their deep effects on interferometric measurements in the near and mid-infrared are reported (Mennesson et al. 2002; Perrin et al. 2004b,a; Schuller et al. 2004; Cotton et al. 2004; Ohnaka 2004b). In general, these layers are believed to extend out to about $2-3 R_*$ and to have temperatures ranging from 1500–2500 K. The photospheric radius of OH26.5+0.6 is of the order of 5–10 mas. From Figure 6.9, it is clear that this does not reduce the correlated flux by a sufficient amount: the increase in radius (which lowers the correlation) is countered by the increase in total flux at 8 micron, due to the lower effective temperature. Therefore, if molecular layers are to be the explanation of the negative detection of fringes, they should extend much further out and be far cooler than generally found for Mira variables. Given the increase in mass-loss of OH/IR stars w.r.t Mira variables, and the correlation between molecular opacity and mass-loss nowadays assumed, this is a plausible explanation. Unfortunately, molecular layers of such a size and temperature will influence the observed FWHM at 8 and 13 μm much in the same way as a dust shell which starts much closer to the central star. We find that this is not compatible with the MIDI FWHM.

6.4.2 A central disk embedded in an outflow

Although the SED is compatible with a *spherically symmetric* model, the assumption of a spherically symmetric dust shell might be strongly violated, as suggested by the asymmetry seen in the acquisition image. It is intuitively clear that a dusty disk embedded in the outflow could account for part of the discrepancies between model and observations: if the MIDI slit was oriented along a nearly edge-on disk, the very high density (and thus opacity) would explain both the large size in the wings of the silicate feature and the non-detection of fringes. Whether this is compatible with the depth of the silicate absorption in the MIDI spectrum depends on the temperature distribution in the disk. Because of the much larger complexity of 2D CSE modelling, we leave an in-depth analysis of this hypothesis to a future dedicated paper. These prospects are discussed in Section 6.5.2.

6.4.3 Asymmetry of the circumstellar environment

The drastic changes observed in the circumstellar structure of AGB and post-AGB stars are particularly puzzling. Information on the geometry of the AGB mass loss was first obtained from interferometric maps of OH 1612 MHz maser emission (Booth et al. 1981; Herman et al. 1985; Bowers & Johnston 1990). These, as well as CO radio line maps of a large number of AGB-stars (Neri et al. 1998; Olofsson 1999, and references therein), were consistent with an overall spherically-symmetric mass loss. However, growing evidence for deviation from spherical geometry in OH/IR stars can be found in the literature (e.g. Engels 2002, and references therein). *While this usually concerns asymmetries at large scale, we have shown in this chapter that even the inner regions of the superwind can already show the onset of asymmetry*

What makes the MIDI observations even more interesting is that JU96 demonstrated that the star entered the superwind phase only ~ 200 years ago. This provides an extremely short upper limit to the development of a large scale asymmetry. The MIDI observations therefore suggest that the appearance of asymmetries can occur in a very short time scale.

JU96 and [Fong et al. \(2002\)](#) reported CO observations which did not show any significant deviation from spherical symmetry for OH26.5+0.6, but most of the emission is spatially unresolved (coming mostly from the superwind). On the other hand, the OH 1612 MHz maser emission from [Baud \(1981\)](#) and [Bowers & Johnston \(1990\)](#) presents a clear picture of the clumpy and asymmetric environment OH26.5+0.6. The radio shell of OH26.5+0.6 is certainly one of the most extended and least symmetric known for OH/IR stars. However, the large scale environment of OH26.5+0.6 is crowded, which complicates the extraction of the radio emission. Since this radio emission is sensitive to any anisotropic UV radiation field, [Bowers & Johnston \(1990\)](#) proposed that an external asymmetric UV field is a likely cause for the detected asymmetry around OH26.5+0.6. However, since we find now that *the axis of symmetry of the Mid-IR object is correlated to the large scale anisotropy detected in radio*, it appears more likely that there is a strong internal influence on the shaping of the OH maser. Moreover, [Bowers & Johnston \(1990\)](#) detected some hints of rotation at low projected velocity ($v_r < 3 \text{ km s}^{-1}$) with a rotational axis aligned with the minor axis of the mid-IR image. It is therefore likely that this rotation is also present much closer to the central star and thus supports the disk+outflow hypothesis.

What could be the origin of the development of such an asymmetry? It is not in the scope of this chapter to review all the mechanisms invoked for explaining such a phenomenon and the reader is invited to consult the review from [Balick & Frank \(2002\)](#). A very popular hypothesis is that a companion (or even a planet) could bias the outflow to the orbital plane. OH26.5+0.6 is not a known binary, but owing to the difficulties to study the central stars of OH/IR stars, this lack of detection is not meaningful. The discussion above leads us to think that the particular characteristics of OH26.5+0.6 are perhaps better understood under the binarity hypothesis. On the other hand, it has been suggested that the rotation of a single central star might be sufficient to bias the outflow to the plane perpendicular to the rotation axis (e.g. [Reimers et al. 2000](#)).

6.4.4 Envelope clumping

The fact that no fringes have been detected from OH26.5+0.6 implies also that the dusty environment of OH26.5+0.6 is relatively homogeneous and smooth. Most of the flux originates from the dust shell and the absence of fringes is in great contrast with the almost ubiquitous fringes found around the central source of the massive object Eta Car in an area as large as $0.6'' \times 0.6''$ with photometric fluxes comparable to the ones reported here ([Chesneau et al. 2005](#)). The use of continuous dust distribution when modelling the circumstellar environment of OH26.5+0.6 is thus fully justified.

6.5 Conclusions and prospects

In this section, we summarize the results presented in this chapter, and present the follow-up observations we already prepared.

6.5.1 First results

The MIDI data presented in this chapter have provided us with 3 different kinds of information on the inner dust shell of OH26.5+0.6:

- The acquisition images at $8.7 \mu\text{m}$ spatially resolve the object in 2 dimensions and show a significant asymmetry with a FWHM ratio of about 0.75 at a scale of a few hundred milli arcseconds. Furthermore, this asymmetry is aligned with that found earlier in the 1612 MHz OH maser, which probes much larger scales than the IR data presented here. The latter asymmetry may therefore not be mainly due to an anisotropic UV radiation field external to OH26.5+0.6. Furthermore, the fact that the asymmetry is found so close to the central star in a $\sim 15 \text{ km s}^{-1}$ wind, implies that deviations from spherical symmetry occur at very short timescales.
- The size of the object in the direction of the slit, i.e. along its major axis, depends strongly on wavelength, with the object being much larger in the silicate feature. This maximum size can be reproduced with a typical spherical dust shell model, based on a fit of the SED at minimum light. However, the object is much larger in the wings of the silicate profile than predicted by the dust shell model. This could indicate either a larger dust inner radius than generally assumed, or an optically very thick object, such as an optically thick dusty disk embedded within the outflow. The latter hypothesis could also explain the observed asymmetry.
- The negative detection of fringes in the interferometric signal suggests that either there is no compact object to be seen within the dust shell, or that the compact object is fairly hot (above 4500 K). The latter hypothesis seems at odds with the observed regular and strong pulsations. The former requirement could be met by the dusty disk.

Clearly, these new observations have raised more questions than they solved. Therefore, more elaborate modelling and new observations are required to pinpoint the exact nature of the inner regions of the dust shell of OH26.5+0.5. We present the strategy behind these new observations in the following section.

6.5.2 Future work

The observations presented in this chapter show that the inner dust shell of OH26.5+0.6 can be spatially resolved using just one Unit Telescope in the N-band. However, these data yield a 2-D image only at one wavelength ($8.7 \mu\text{m}$), and the spatial resolution is not sufficient to actually see the inner edge of the dust envelope. Moreover, the spectral resolution is too low

to observe any spectral features in the wings of the silicate profile, which could possibly point at a molecular nature of the extra source of opacity.

It is therefore obvious that the investigation on OH26.5+0.6 could progress by means of 2 new sets of observations: (1) VISIR observations in the thermal IR and (2) Adaptive Optics (AO) imaging in the near-IR with NAOS-CONICA on Yepun (UT4).

6.5.2.1 Proposed VISIR observations

VISIR observations of OH26.5+0.6 are proposed within the Guaranteed Time for Observations (GTO) program “VISIR OBSERVATIONS OF EVOLVED STARS”. These will allow both 2-D imaging of the inner dust shell at different wavelengths in the N-band, to study the asymmetry of the shell, and also high-resolution spectroscopy to identify the source of opacity in the wings of the silicate profile. These observations will take place in P75 (1 April through 1 October 2005).

6.5.2.2 Proposed NAOS-CONICA observations

These near-IR AO observations have a spatial resolution which is an order of a magnitude higher than that of the data presented in this chapter. Depending on the nature of OH26.5+0.6 (spherical with or without reduced mass-loss, disk+outflow), we expect to see strong differences in the spatial intensity distribution between the filters available with NACO on a scale of a few hundred milli-arcseconds. Model predictions range from almost no scattered light and just a small core of thermal emission in all filters (model with a large inner hole, upper panel of Figure 6.10), over a source which shows only in J a significant amount of scattering (lower panel of Figure 6.10), to an image with a thermally emitting disk and a large halo of scattered light in J, H, K and possibly even at larger wavelengths (the case of an optically very thick disk). Furthermore, we expect to see directly the outer boundary of the superwind at about 0.2-0.5'' in the filters dominated by thermal emission.

We therefore proposed to take deep images in J, H, K, L' and M, which will allow us to determine the true geometrical nature of the superwind. The proposal was accepted and the requested 6 hours of observing are scheduled for the night between May 17 and 18, 2005.

Obviously, OH26.5+0.6 is very reddened by its circumstellar environment. Its mean magnitudes through the pulsation cycle are $m_J = 17.0$, $m_H = 14.6$, $m_K = 8.0$, $m_{L'} = 1.3$ and $m_M = -0.7$. This imposes a certain strategy for the observations:

- Obtaining images in K, L' and M of OH26.5+0.6 and a PSF calibrator (HD 171610) in order to check that the central source is resolved. For each image, the flux ratio F_{star}/F_{dust} will be estimated. From these three images, the total dust opacity will be determined and compared with several models in order to get an estimation of the (hot) dust column density and distribution.
- After a careful PSF subtraction, the (thermal) emission from 0.5 to 3-5'' will be estimated, allowing us to directly image the outer boundary of the superwind. We are quite confident that the brightness of the source will provide a sufficiently good correction from the

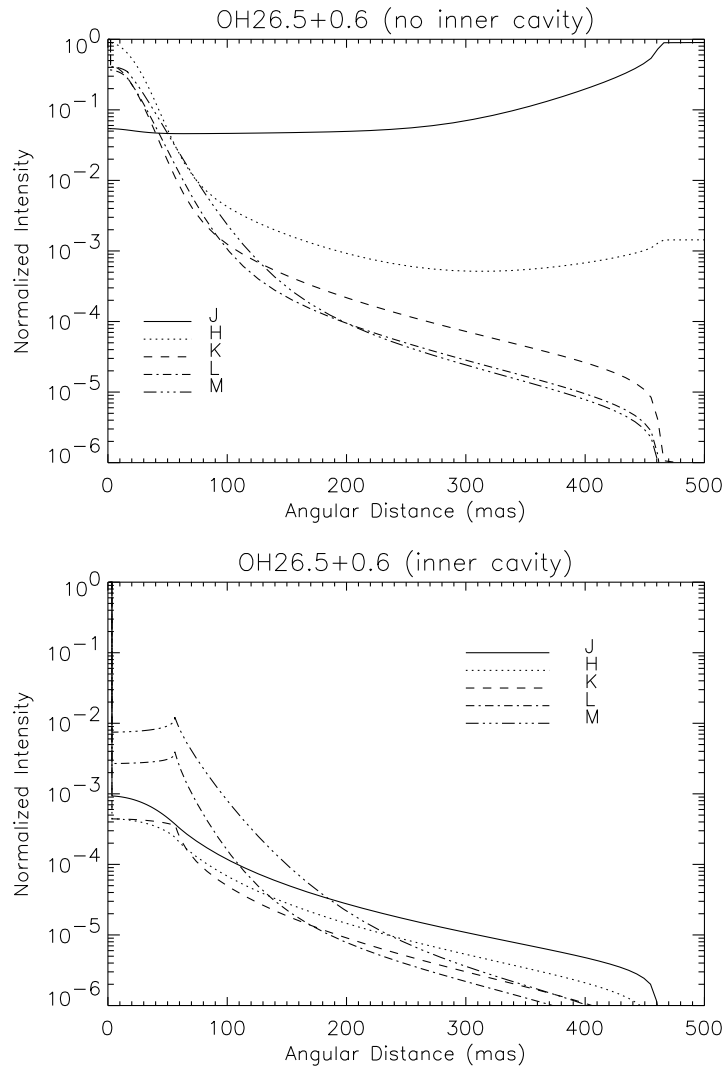


Figure 6.10— Upper panel: extensions of the stellar environment of OH26.5+0.6 based on a dust shell model derived from the SED alone (JU96 model). Lower panel: alternative model derived when the MIDI constraints on the dust shell extension between 8 and $13.5 \mu\text{m}$ are taken into account. This model implies an inner radius greatly increased ($20 R_{\star}$) compared to the previous model ($8 R_{\star}$).

Adaptive Optics NAOS to allow such a difficult task.

- An image in J and H will be performed to measure the flux from the central source and get an estimation of the scattered light around the object. Owing to the faintness of the source at these wavelengths, the dynamic range will be limited and no PSF observations are foreseen.

Altogether, these 3 datasets will hopefully move our understanding of the very late AGB a (few) step(s) ahead.

